MIT Open Access Articles

Combinatorial study of thermal stability in ternary nanocrystalline alloys

Full length article

Combinatorial study of thermal stability in ternary nanocrystalline alloys

Sebastian A. Kube[a], Wenting Xing[b], Arvind Kalidindi[b], Sungwoo Sohn[a], Amit Datye[a], Dor Amram[b], Christopher A. Schuh[b], Jan Schroers[a],*

[a] Department of Mechanical Engineering and Materials Science, Yale University, 15 Prospect Street, New Haven, CT 06511, United States
[b] Department of Materials Science and Engineering, Massachusetts Institute of Technology, 77 Massachusetts Avenue, Cambridge, MA 02139, United States

ABSTRACT

Nanocrystalline alloys can be stabilized through selective grain boundary segregation of specific solute element additions. Increasing attention is being paid to ternary and higher order systems, where complex interactions govern segregation. To efficiently study the large composition spaces of such systems, we apply a high-throughput combinatorial technique revealing nanocrystalline stability through composition-grain-size maps. We compare two systems with distinct binary and ternary alloy interactions: In Pt–AuAg both binaries are expected to be stable, whereas in Pt–AuPd the Pt–Pd binary is unstable and Au-induced co-segregation of Pd was previously reported. For ternary Pt–AuAg we find excellent thermal stability throughout. The Pt–AuPd system, by contrast, divides into an unstable regime, where Pd solute dominates and precipitates, and a stable regime, where Au solute dominates and retains Pd in the grain boundary. Overall, by combining current theory and the introduced combinatorial approach, stable multicomponent nanocrystalline composition spaces can be rapidly determined.

© 2020 Acta Materialia Inc. Published by Elsevier Ltd. This is an open access article under the CC BY-NC-ND license.
(http://creativecommons.org/licenses/by-nc-nd/4.0/)

1. Introduction

Alloys often exhibit enhanced properties in their nanocrystalline state, where grains are typically smaller than 100 nm (e.g. [1,2]). These include superior mechanical performance in terms of high strength, plasticity and wear resistance [3–12], a high coercivity and softness in magnetic materials [13–16], and excellent thermoelectric properties [17–19]. The large volume fraction of grain boundaries in nanocrystalline alloys, however, is usually associated with a significant energetic penalty. Such nanostructures are unstable and their grains quickly coarsen even at low homologous temperatures [3,20]. Effective stabilization against coarsening is therefore a key challenge for practical implementation.

One effective stabilization strategy first proposed by Weissmüller and further developed in the prior work of some of the present authors, is grain boundary alloying [3,20–24]: In this approach, the grain boundaries are thermodynamically stabilized by specific solute species, which preferentially occupy grain boundary sites due to a high enthalpy of grain boundary segregation. This reduces the grain boundary excess energy and can even stabilize the nanocrystalline configuration relative to competing phases such as intermetallics [3,20–24]. Additionally, solute segregation often hinders grain growth kinetically by impeding grain boundary motion [25,26].

On this basis, various binary systems have been reported with a stable nanocrystalline structure, such as W–Ti, Cu–Ta or Ni–W [3,27–29]. Such systems also experimentally support the theoretical prediction that the grain size can be tuned: For a given solute concentration a grain size exists, for which optimal solute saturation of the corresponding grain boundary area is achieved. With increasing solute concentration, a larger grain boundary area is needed for optimal saturation and so the equilibrium grain size decreases [3,20–23,27,30].

Recently, there has been growing interest in understanding the nature of ternary and multicomponent nanocrystalline systems. This is motivated by the limited number of practical binary alloy combinations with favorable constituent interaction and by recognizing that alloys with two or more solute species can be tuned towards a combination of desired properties within a wider design space [31–38]. A theoretical treatment of such systems becomes significantly more complex as both the number of underlying pairwise interactions as well as possible configurational outcomes, that need to be accounted for, increase exponentially with the number of constituents [31,39–44]. Earlier work has developed a theoretical framework for multicomponent grain boundary segregation, presented schemes to identify promising ternary alloy systems based on the underlying binary systems, and conducted preliminary experimental investigations into ternary effects [25,39,45]. While quantitative modeling of multicomponent nanocrystalline alloys is evolving, it has been limited, as it is generally not straightforward, little tested for experimental agreement, and relying mostly on estimates of constituent interactions and assumptions regarding the grain boundary structure.

Meanwhile, direct observations of the grain boundary segregation state and structural stability are accessible in experiments. These could be used to better calibrate the many unknowns in models, but are hard-won data studying one composition at a time. Experimental work is particularly challenged with the large multicomponent composition space,

that requires exponentially more effort to study as the number of components increases in a system. In such cases, high-throughput methods have proven effective for fast and efficient screening. One such method is based on combinatorial co-sputtering, where hundreds of compositionally distinct alloys are fabricated in parallel, followed by automated compositional and structural characterization. This method has generated large data sets and provided significant insight across a wide range of alloy development questions covering alloy classes such as Shape Memory Alloys, High Entropy Alloys and Bulk Metallic Glasses, as well as their phase stabilities and properties [46–57].

Motivated by the above, here we employ a combinatorial co-sputtering technique to study the thermal stability of nanocrystalline alloys in the alloy systems Pt–AuAg and Pt–AuPd. Relevant energetic interactions and predicted behaviors are summarized in Table 1. Both systems are based on binary Pt–Au, where Pt is the solvent and Au the solute. Pt–Au has been reported to exhibit a stable nanocrystalline structure due to a high enthalpy of grain boundary segregation [25,58–60]. For the two ternary systems we then introduce additional solute species. In one case we add Ag: The large grain boundary segregation enthalpy and negative mixing enthalpy of Ag suggest that the Pt–Ag binary should exhibit a similarly strong segregation tendency as Pt–Au and good nanocrystalline stability. Au and Ag display no appreciable solute-solute interaction and should interact in a simple substitutional fashion [25]. Based on these underlying binary interactions, we hypothesize that alloys in the Pt–AuAg ternary system should display high nanocrystalline stability. In the other case we add Pd: Suggested by its low segregation enthalpy and previous experimental reports [45], desegregation and unstable nanocrystalline structure are expected in the Pt–Pd binary. In the Pt–AuPd ternary system, however, the presence of Au can induce the co-segregation of Pd to the grain boundary and produce a more stable nanocrystalline structure (as shown for $Pt_{76}Au_{18}Pd_6$ at 400°C in our previous work [25]). This is attributed to an enhanced effective segregation enthalpy of Pd when Au is enriched at the grain boundary. When the amount of Pd outweighs Au, however, the co-segregated state is lost, Pd precipitates and grains coarsen (observed for $Pt_{54}Au_{10}Pd_{36}$ at 400°C [25]). Given this particular solute-solute interaction, we hypothesize that the Pt–AuPd ternary alloy system may exhibit nanocrystalline stability for the composition range where sufficient Au is present to retain Pd in the co-segregated state, but lose stability for higher ratios of Pd:Au.

Building on the insights gained in previous work and the hypotheses developed above, we use the combinatorial approach to compare the thermal stabilities of nanocrystalline Pt–AuAg and Pt–AuPd. Most of the alloys considered here, in particular those in the Pt–AuAg system, have never been studied in terms of their grain size and thermal stability. An overview of the experimental approach is presented in Fig. 1. In the first step, we use co-sputtering to fabricate two alloy libraries for each system. These libraries contain ~170 compositionally distinct ternary alloy thin film patches on a sapphire substrate, representing large compositional sections of the Pt-solvent-rich composition space. Using fast-screening energy dispersive X-ray spectroscopy (EDX), we then determine the compositional distribution

across the libraries. In the next step we characterize the structural changes induced in each alloy through annealing. This is achieved through high-throughput X-ray diffraction (XRD), where X-ray diffractograms are acquired for each alloy patch in the as-sputtered state (AS), after annealing at 400°C for 24 hrs, and after annealing at 800°C for 24 hrs. We then analyze the diffractograms qualitatively and quantitatively. In particular, we use the Scherrer equation (Eq. (1)) to determine grain size values from the observed peak widths. This allows us to generate composition-grain-size maps in order to draw conclusions on the thermal stability of the nanocrystalline configuration as a function of the ternary composition. For selected compositions we confirm the experimental observations presented in those maps using scanning electron microscopy (SEM).

2. Experimental

2.1. Combinatorial co-sputtering

The compositional alloy libraries were fabricated using confocal DC magnetron co-sputtering (AJA International ATC2200). The sputtering targets Pt, Au, and Ag/Pd were loaded into three sputtering sources, which are arranged tetrahedrally towards the substrate, pointing at its center at an angle of 29.8° (cf. sputtering schematic in Fig. 1). The power of the sputtering plasma and accordingly the deposition rate were adjusted on each source to yield an approximate center composition of
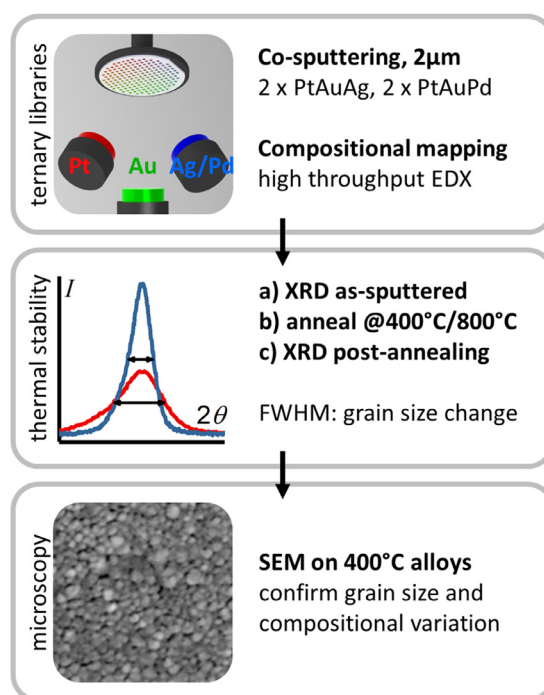

Fig. 1. Workflow of study. *Ternary libraries:* For each system, Pt–AuAg and Pt–AuPd, two compositional libraries are fabricated using combinatorial co-sputtering to a film thickness of 2 μm, spanning a large section of the Pt-rich ternary composition space. Using fast-screening EDX, this compositional distribution is mapped from composition reference libraries, which were fabricated under identical sputtering conditions as the main libraries. *Thermal stability:* Using high-throughput XRD, diffractograms are acquired for ~170 different compositions in the as-sputtered state and after annealing at 400°C and 800°C for 24 h. Qualitative diffractogram analysis reveals present phases. Quantitative analysis focusing particularly on the observed peak widths (FWHM) using the Scherrer equation (Eq. (1)) reveals the dependence of the grain size on the composition and processing condition. In order to limit substrate-film interdiffusion during annealing, sapphire substrates were chosen for their high thermal stability. To avoid significant intra-film diffusion and an associated loss of the compositional gradient, the film was deposited in small patches, with the gaps in between acting as long-range diffusion barriers. *Microscopy:* SEM was conducted on alloys annealed at 400°C to confirm the compositional variation of grain sizes determined through XRD. (For interpretation of the references to color in this figure legend, the reader is referred to the web version of this article.)

Table 1
Expected behaviors, binary enthalpies of mixing and grain boundary segregation, and effective enthalpy of co-segregation in the Pt–AuAg and Pt–AuPd ternaries based on Miedema estimates [58,61,62] and existing experimental observations.

		Pt–AuAg	Pt–AuPd
Predicted behavior	in binary: A-B	segregation	segregation
	in binary: A-C	segregation	desegregation
	in ternary: B-C	weak interaction	Au-induced co-segregation of Pd
Mixing enthalpy [kJ/mol]	ΔH^{mix}(A-B)	+19.3	+19.3
	ΔH^{mix}(A-C)	−2.6	+8.2
	ΔH^{mix}(B-C)	±0.0	−6.7 [63]
Segregation enthalpy [kJ/mol]	ΔH^{seg}(A-B)	+26.4	+26.4
	ΔH^{seg}(A-C)	+27.5	+11.9
	$\Delta H^{seg-eff}$(A-C)	NA	+17.8 [45]

$Pt_{70}Au_{15}Ag_{15}$ and $Pt_{70}Au_{15}Pd_{15}$, respectively. The sputtering target purities were 99.99% or better (Kurt Lesker Company and APMEX Inc.). For fabricating the main libraries used in thermal testing, the alloy films were deposited in patches on a 0.25″ spaced square grid through a 0.01″ thick steel mask to a thickness of 2 μm on 100 mm diameter sapphire wafers (University Wafer Inc.). For fabricating the composition reference libraries used in EDX mapping, sputtering conditions were maintained identical to the main libraries, except the continuous films were deposited to a thickness of 300 nm on unmasked 100 mm diameter silicon wafers (University Wafer Inc.). Before each co-sputtering fabrication, the processing chamber was evacuated to a base pressure of 5.0E−7 Torr or less. The films were then deposited under flowing ultra-high purity argon at 5.8E−3 Torr.

2.2. Library characterization

Composition distribution maps of the composition reference libraries were determined on a 5 mm spaced square grid across the wafers using automated EDX (Oxford Instruments X-Max detector attached to a Zeiss Sigma VP Field Emission scanning electron microscope). The composition data were calibrated based on bulk samples with the known compositions $Pt_{69.92}Au_{15.04}Ag_{15.04}$ and $Pt_{70.01}Au_{14.94}Pd_{15.05}$. Since the on-wafer coordinates of the main sample alloy patches differ from the EDX grid coordinates, the compositions of the main sample alloy patches were computed through bilinear interpolation from the four closest surrounding EDX grid compositions.

X-ray diffractograms of the as-sputtered and annealed alloys within the main libraries were acquired on a subset of alloy patches (~170 compositions spanning across a library, consistent between the main libraries). Measurements were conducted on a Rigaku Smartlab X-ray diffractometer using Bragg-Brentano focusing, Cu-Kα radiation, a 2 mm beam mask, and an automated xy-stage. The substrate was tilted out of the detection plane by 15°, in order to eliminate the background signal from the single-crystalline substrate. Subsequent diffractogram regressions were performed on the background-corrected diffractograms using MatLab's "fit" function. An instrumental angular resolution of better than 0.05° allowed for a highly resolved analysis of the compositional variation of lattice constants. Quantification was omitted where ambiguous and low-quality fits were obtained.

2.3. Library annealing

The main libraries were annealed in a tube furnace (Across International TF1600). In preparation, the sealed tube was purged multiple times by first evacuating to 20 mTorr and then flooding with ultra-high purity argon. The temperature was then ramped at a rate of 200°C/hour and the samples were annealed in flowing ultra-high purity argon for 24 h at 400°C and 800°C, respectively. Given the inert atmosphere and the noble nature of the films' constituent elements, the samples did not notably oxidize under either condition. Upon completion, the tube was left to air-cool to room temperature before the samples were unloaded. Possible thermal stresses arising upon cooling from annealing to room temperature are not expected to significantly interfere with the following data analysis. Given the rather similar thermal expansion coefficients of sapphire and the alloys' base element platinum (8.11×10^{-6} K^{-1} [64] and 8.8×10^{-6} K^{-1} [65], respectively), estimated film strains and associated stresses are negligibly small. Further, the metallic film patches display no visibly altered substrate adhesion following thermal treatment.

2.4. SEM

Scanning electron micrographs were acquired using a Hitachi CFE SU8230 scanning electron microscope. Micrographs were obtained for 200kx magnification at an accelerating voltage of 5 kV.

3. Results and discussion

3.1. Qualitative examination of diffraction data

A representative overview of the diffractograms grouped by processing condition is provided in Fig. 2 and Fig. S1 for the Pt−AuAg and Pt−AuPd system, respectively. First inspection reveals Bragg diffraction peaks corresponding to FCC structures, as expected for the FCC constituent elements. The relative intensities of the diffraction peaks agree well with the typical FCC pattern, suggesting no crystallographic texture. This is indicative of the nanocrystalline configuration in the film, where compared to the ~2 μm thick film the small grain size results in a large statistical sample size and only a small fraction of grains lies within the texturing field of the substrate.

In the Pt−AuAg system (Fig. 2), the diffractograms obtained for as-sputtered (AS) and 400°C annealed samples for a given composition are very similar, indicating that annealing at 400°C induces only minor structural changes. The diffractograms feature two sets of broad overlapping peaks, which are offset by only a small angle (cf. also Fig. 3): The primary set of peaks lies at higher diffraction angles corresponding to smaller lattice constants, is narrower, and decreases in overall intensity for increasing solute concentration. This can be attributed to a primary and more coarse-grained phase which is rich in Pt solvent, as Pt has the smallest FCC lattice constant in the system (cf. Table 2). The secondary overlapping set of peaks appears as shoulders on the lower diffraction angle flanks of the primary set. It corresponds to larger lattice constants, is broader, and increases in overall intensity for increasing solute concentration. It is therefore attributed to a secondary region of Au and Ag solute-enriched FCC material with a smaller grain size or correlation length, of which the volume fraction appears to increase for higher nominal solute concentrations. Overall, both peak sets are very broad and indicate a nanocrystalline microstructure.

What is the meaning of this secondary peak set found for AS and 400°C? The solute elements Au and Ag were specifically chosen for their preference to segregate from the Pt solvent and occupy the grain boundary region. We thus assume that the primary peaks correspond to the main solvent-rich FCC phase, in which by design we want to achieve a thermodynamically stabilized nanocrystalline state, whereas the secondary peaks may correspond to the segregant enriched grain boundary regions. As the solute concentration increases, more solute can segregate, by which the volume fractions and the relative diffraction intensities of the secondary, grain boundary affiliated peaks increase.

The diffractograms obtained for 800°C are different from AS and 400°C. Now, two clearly distinct FCC phases separate out; their peaks have significantly narrowed and no longer overlap. The reduced peak widths suggest that the corresponding grains have coarsened beyond ~100 nm. Further, the diffraction angle offset and the corresponding lattice constant difference between the two peak sets have significantly increased (from $\Delta a_{AS} \approx 0.03$ Å and $\Delta a_{400\ °C} \approx 0.03$ Å to $\Delta a_{800\ °C} \approx 0.11$ Å, cf. Figs. 2 and 4 and Fig. S2), suggesting that both phases have significantly enriched in their respective dominant constituent elements during annealing at 800°C. From these observations we conclude that upon annealing of the as-sputtered samples at 800°C, the nanocrystalline configuration is lost as grains significantly coarsen and decomposition into separate Pt and AuAg phases occurs, of which the lattice constants match the literature values (Table 2). Accordingly, the relative diffraction intensities of both phases vary depending on the concentrations of Pt versus AuAg. Also, this phase separation is in agreement with the binary and ternary equilibrium phase diagrams for these elements at 800°C. Finally, such a loss of nanocrystalline structure is common in grain-boundary stabilized alloys with competing phases [25].

While the above discussion focuses on the diffractograms obtained for the Pt−AuAg system as illustrated in Fig. 2, similar observations are made for the Pt−AuPd system (Fig. S1). Unlike Au and Ag, however, the FCC lattice constant of Pd lies very close to Pt (cf. Table 2). Therefore, for Pd-rich compositions in the as-sputtered and 400°C annealed states, the
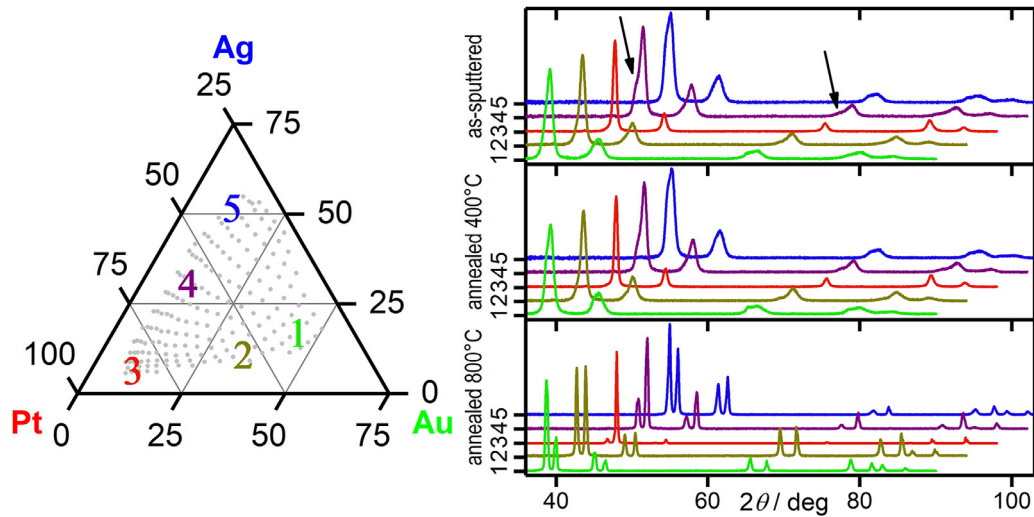
Fig. 2. Selected X-ray diffractograms for five representative compositions in the Pt–AuAg system grouped by processing condition. (Compositions in at.%. An equivalent figure for the Pt–AuPd system is provided in Fig. S1.) *As-sputtered and annealed at 400 °C:* Diffraction peaks from a primary FCC phase are found in the Pt-rich region (composition 3). As the solute concentration increases (Au-rich: 3–2–1; Ag-rich: 3–4–5), a shoulder grows on the left flank of the primary peaks (see examples highlighted by black arrows), which arises from a broad overlapping diffraction peak that is centered at slightly smaller diffraction angles. It therefore corresponds to a secondary FCC structure with a slightly larger lattice constant. Since the lattice constant of Pt is smaller than for Au and Ag (cf. Table 2), the primary peak set is interpreted as the Pt solvent rich grain interior, from which with increasing nominal solute concentration an increasing amount of Au and Ag segregates to the grain boundary region producing the secondary peak set. Overall, the primary diffraction peaks are broad and appear to broaden with increasing solute concentration, suggesting a decrease in grain size. *Annealed at 800 °C:* Two sets of narrow and non-overlapping FCC peaks are found. This suggests that full phase separation and significant grain coarsening occur during annealing at 800°C. In agreement with Table 2, the primary phase found at higher diffraction angles (i.e. $2\theta_{(111)} \approx 39.93°$, $a_{FCC} \approx 3.91$ Å) is interpreted as Pt phase, whereas the secondary phase (i.e. $2\theta_{(111)} \approx 38.78°$, $a_{FCC} \approx 4.02$ Å) is interpreted as AuAg phase. This is consistent with the corresponding equilibrium phase diagrams, which indicate that Pt at 800°C demixes from both Au and Ag, whereas the latter form a solid solution across all binary compositions. (For interpretation of the references to color in this figure legend, the reader is referred to the web version of this article.)
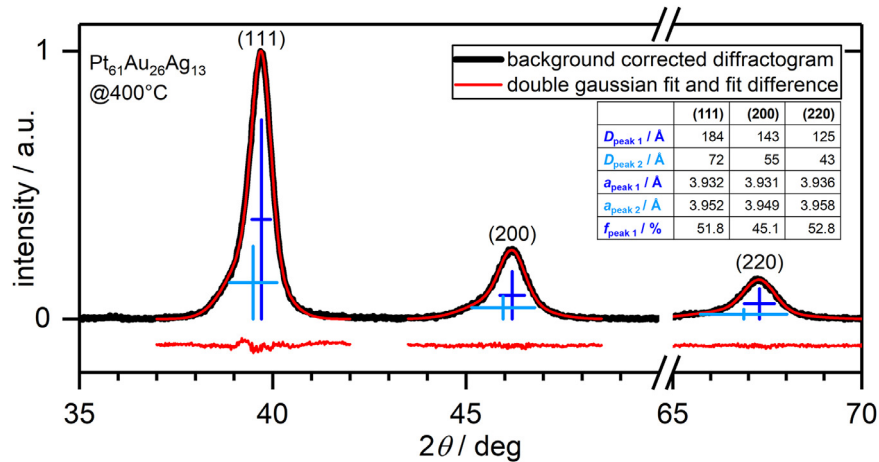

Fig. 3. Quantitative analysis of diffractograms: Deconvoluting and quantifying the primary and secondary peaks through regression, as exemplified for Pt$_{61}$Au$_{26}$Ag$_{13}$ annealed at 400°C: Regression of a double gaussian function (additive superposition of two independent gaussian curves) is performed on the overlapping primary and secondary (111), (200), and (220) double diffraction peaks. Close agreement between the fit-function and the diffraction data is achieved, as indicated by the flat fit difference curves. Position, width, and height of the individual primary and secondary Gaussian curves are indicated in blue for each regression. From these, structural characteristics can be extracted for each peak set, as listed in the inset table (D_i, the grain size/coherence length; a_i, the FCC lattice parameter; f_i, the fraction of diffracted intensity contributed by the individual peaks to the convolution, which is not equal to the phase volume fraction, but a function thereof). For some compositions, particularly Pt–AuAg at high solute concentrations, accurate regressions could not be performed and quantification was not conducted. (For interpretation of the references to color in this figure legend, the reader is referred to the web version of this article.)

secondary diffraction peaks are no longer clearly discernible. Also, unlike the Pt–AuAg system, particularly in the Pd-rich composition region, a visible narrowing of the diffraction peaks occurs during annealing at 400°C, which indicates significant grain coarsening in this region. Finally, for Pt–AuPd annealed at 800°C it is unclear whether Pt and Pd demix into separate phases or form a solid solution together, where the latter is suggested by their equilibrium phase diagrams.

3.2. Quantitative examination of diffraction data, as-sputtered and annealed at 400°C

In the as-sputtered and annealed at 400°C states, the broadly overlapping primary and secondary diffraction peaks prohibit a direct

measurement of peak widths and a subsequent grain size calculation. To quantify the diffractograms these peaks must first be deconvoluted and then analyzed for their individual contributions. For this purpose, we perform a regression on the (111), (200), and (220) double diffraction peaks (Fig. 3). The diffractogram is fitted with a double Gaussian function, i.e. two independent and additively superimposed Gaussian curves. Fit parameters include firstly the primary and secondary peak position revealing the respective lattice parameters a_i, secondly the peak width used to calculate the respective grain size D_{hkl}, and thirdly the respective peak area used to determine the relative intensity contributions f_i to the convoluted diffraction peak. The grain size D_{hkl} for the given set of lattice planes is then calculated using the Scherrer equation (Eq. (1)), where $\lambda = 1.5418$ Å is the

Table 2

Selected properties for the elements in this study: Atomic radii [66], corresponding FCC lattice constants a_{FCC}, melting temperature T_M [67] and electron densities ED [67].

	Element	Radius (Å)	a_{FCC} (Å)	T_M (°C)	ED (mol cm^{-3})
Solvent	**Pt**	1.39	3.93	1772	8.58
Solute 1	**Au**	1.44	4.07	1064	7.75
Solute 2	**Ag**	1.44	4.07	962	4.57
	Pd	1.37	3.87	1555	5.20

The lattice constants measured and presented for the alloys in this study slightly deviate from these literature values. E.g., $a_{phase\ 1}$ in Fig. 4(d) passes below the literature value of Pt, the smallest constituent. This is attributed to some variation of the values reported in the literature. For data interpretation, the focus here lies on the relation of the atomic radii to each other, which is consistently reported in the literature in agreement with the values listed below. ED values were calculated based on the elemental molar densities and electron numbers.
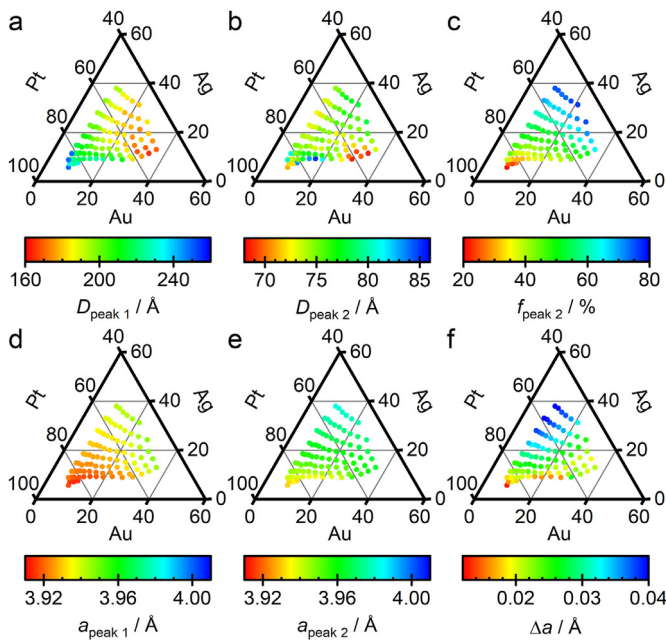

Fig. 4. Gibbs triangle maps showing the compositional distribution (at.%) of extracted quantities for alloys in the Pt−AuAg system at 400°C (equivalent plots for Pt−AuAg AS, Pt−AuPd AS, and Pt−AuPd 400°C provided in Figs. S2−S4): (a) Size from primary peak (grain interior): With increasing solute concentration, $D_{peak\ 1}$ decreases from 260 Å to 160 Å. (b) Size from secondary peak: $D_{peak\ 2}$ lies between 70 Å and 80 Å and exhibits no significant variation with composition. (c) Fraction of diffracted intensity contributed by secondary peak: With increasing solute concentration, $f_{peak\ 2}$ grows from 20% to 80% as an increasing volume fraction of solute-rich grain boundary regions is formed. (d/e) FCC lattice constants of the primary and secondary peaks (plotted to same color scale): $a_{peak\ 1}$ and $a_{peak\ 2}$ grow with increasing nominal concentration of the comparatively large solute elements. (f) Absolute difference of FCC lattice constant between the primary and secondary peak: Δa varies over a range of about 0.01−0.04 Å. This difference is small compared to values of about 0.11 Å, as observed for the demixed state at 800°C. Such small Δa suggests that the grain interior and grain boundary region at 400°C are compositionally close compared to the fully demixed state. Yet, comparing between the solutes Au and Ag, Δa grows noticeably towards higher concentrations of Ag, suggesting that compositional segregation is more pronounced here. (For interpretation of the references to color in this figure legend, the reader is referred to the web version of this article.)

probing wavelength for Cu K$_\alpha$ radiation, β is the peak width in radians, and θ is half the diffraction angle [68−70].

$$D_{hkl} = \frac{0.94\ \lambda}{\beta\ \cos\theta} \qquad (1)$$

Strictly speaking, D_{hkl} does not correspond to the actual grain size, but to the coherence length of the grains under the given measurement conditions. Lattice defects, such as stacking faults, can contribute to a discrepancy between grain size and coherence length. However, this discrepancy typically becomes small for nano-sized grains. At the same time, the grains obtained here are not equiaxed, but somewhat

elongated along the columnar growth direction [25,45]. However, the diffractograms were measured with the substrate tilted at 15° out of plane, so measuring the size of the elongated grains preferentially samples the grain widths rather than the long axis length. Therefore, D_{hkl} here approximately corresponds to the columnar diameter, the values of which are in good agreement with those determined through TEM in our previous work, as discussed below. The performed regression yields close agreement between the experimental data and the fit function (Fig. 3). For a number of compositions, particularly solute rich compositions in Pt−AuAg, quantification was not conducted because accurate regressions could not be performed. Close agreement of the extracted quantities is found between the (111), (200), and (220) diffraction peaks (cf. inset table in Fig. 3). The determined grain sizes D_i decrease slightly towards the higher peaks, which we attribute to a non-spherical average grain shape and the approximate character of the Scherrer Equation. Consistent values are also obtained for a_i and f_i, where the latter is remarkable in a thin film with some degree of expected texturing. Given this strong overall consistency, in the following we will focus on the specific results extracted from the (111) diffraction peaks. The trends reported, however, are similarly observed for all three lattice planes.

By merging the data extracted from the diffractograms with the compositional EDX data, we now generate Gibbs triangle maps showing the compositional variation of the structural quantities, as exemplified for Pt−AuAg at 400°C in Fig. 4 (all other data provided in Supplementary material). Fig. 4a shows the grain size of the primary Pt-rich phase, which sets out at about 26 nm and decreases to about 16 nm with increasing solute concentration.

The secondary peaks which arise from solute-rich regions are not clearly associated with a grain structure yet, but we suggested above that they may be associated with the grain boundary regions, as a segregation layer or perhaps even a wetting layer of solute. In Fig. 4b, the length scale obtained from Scherrer analysis may therefore rather correspond to the characteristic size of such a region. The extracted values are around 7−8 nm and display no significant compositional variation; this length scale may be related to the width of the solute segregation zone around the boundary, and is comparable to observations of grain boundary enrichment in Pt$_{76}$Au$_{18}$Pd$_6$ through STEM/EDX in our previous work [25,45]. Combined with the qualitative observations from Section 2.1, we conclude that Au and Ag segregate from Pt to the grain boundary regions. Given the large volume fraction of the grain boundary regions under these conditions, the segregate is prominent enough to manifest a secondary peak in the diffractograms. This appears to stabilize the primary Pt-rich grains against coarsening and even dictate a preferred grain size that decreases with increasing solute concentration, as will be further discussed in Section 2.3.

The higher the solute concentration is, the more solute is available to segregate to grain boundaries, which should increase the volume fraction of the grain boundary region accordingly. This is evidenced in Fig. 4c, where $f_{peak\ 2}$, the relative diffraction intensity of the secondary peak, increases from about 20−80%. Of course, the relative diffraction intensity f is not identical to the volume fraction; the primary and secondary peaks diffract from regions that differ in composition and accordingly in their effective scattering strengths. These depend on the specific local compositions, densities, and form factors of constituent elements at the given diffraction angle. While the latter is approximately proportional to an element's electron number and could thus be used to convert from $f_{peak\ 2}$ to proper volume fractions, the local compositions and densities are unknown, making a direct conversion impossible. We can, however, assume that the compositional difference between the grain interior and grain boundary region is relatively small (as confirmed in the following paragraph). According to the electron density values listed in Table 2, a maximum difference in scattering strength of about 2:1 is achieved for hypothetical unmixing into the pure phases (PtAu) and Ag. For grain boundary solute enrichment without phase separation we would then estimate that the actual scattering strength difference is much closer to 1:1. Thus, $f_{peak\ 2}$ closely approximates the volume fraction of the solute-enriched region.

In Figs. 4d-f, the compositional variation of the lattice constants a_i and the absolute lattice constant difference Δa between the two putative compositional regions are shown. With increasing solute concentration, $a_{peak\ 1}$ grows from about 3.91−3.95 Å, $a_{peak\ 2}$ grows from about 3.93−3.99 Å. Δa ranges from about 0.01−0.04 Å. Since in the Pt−AuAg system both solute species have a larger lattice constant than Pt by about 0.14 Å (cf. Table 2), Δa serves as a good indicator of how compositionally distinct the grain interior and grain boundary regions are. Comparing Δa = 0.01−0.04 Å at 400°C to a difference of 0.11 Å for the fully phase separated state at 800°C (Fig. 2) and the maximum possible difference of 0.14 Å (Table 2), we conclude that at 400°C the grain interior and grain boundaries are compositionally relatively close. The secondary peak suggests only partial enrichment in solute, thus confirming our assumption in the above paragraph. Further, we observe that Δa significantly grows towards higher Ag concentrations. This indicates that Ag has an even stronger tendency to form stabilizing segregated regions at grain boundaries than does Au, which may be attributed to the significantly smaller, even negative heat of mixing and the associated higher resistance against precipitation [24].

Observations similar to the above are made in the as-sputtered state and in the Pt−AuPd system, as shown in Figs. S2−S4. In the Pt−AuPd system, a significant difference continues to be that the lattice constant of Pd is not equal to the one of Au, but rather close to Pt. Therefore, Δa no longer indicates how close the compositions of grain interior and grain boundary regions are. Rather, Δa diminishes towards high Pd concentrations (cf. Figs. S3f and S4f), where the primary and secondary peak sets coincide (cf. Fig. S1). For high Au concentrations, by contrast, two offset peak sets are observed and a lattice constant difference of about 0.025 Å is attained. This agrees with the Δa values observed for Au-rich compositions in Pt−AuAg, suggesting that grain boundary compositional differences continue to be minor.

3.3. Compositional dependence and thermal stability of the nanocrystalline state

The above sections provide a description of the nanocrystalline structure across a wide compositional range in both the Pt−AuAg and the Pt−AuPd system in the as-sputtered and both annealed states. We will now examine the structural changes resulting from annealing the as-sputtered samples at 400°C, focusing on the size of the Pt-solvent-rich grains ($D_{peak\ 1}$) as the main indicator of nanostructure stability.

In Fig. 5, compositional maps of the grain size are presented for both systems before and after annealing at 400°C. A striking feature
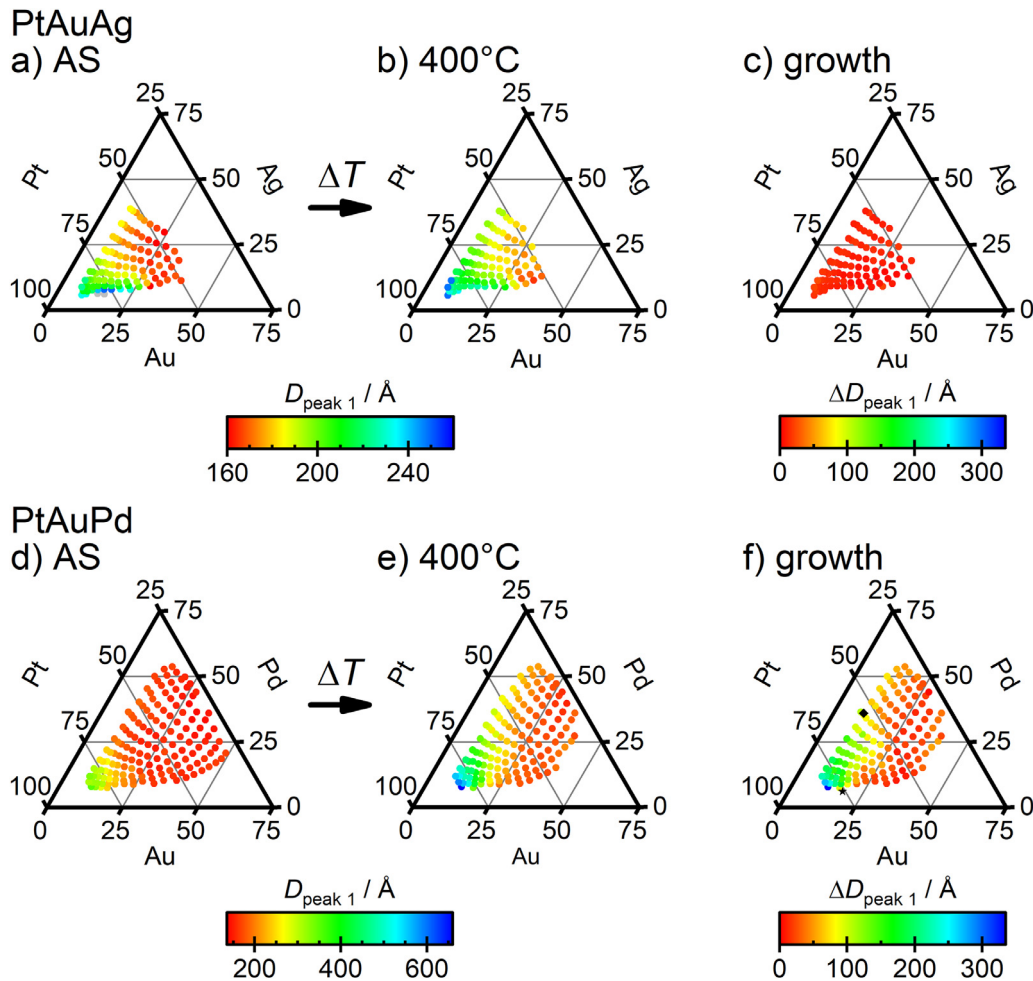

Fig. 5. Comparing thermal stability between systems based on the primary grain size ($D_{peak\ 1}$): (a−c) Grain size distribution as-sputtered, after annealing at 400°C, and absolute grain size change $\Delta D_{peak\ 1}$ in the Pt−AuAg system: Grain sizes change by less than 2 nm, suggesting excellent thermal stability across all compositions. (d-f) Three regimes are identified: Grains grow by less than 5 nm on the side of higher concentrations of Au than of Pd, which is attributed to thermodynamic stabilization. Grains grow by about 15−25 nm for higher concentrations of Pd where combined solute concentrations remain below 50 at.%, because Pd is an ineffective grain boundary stabilizer. Pd does, however, precipitate to the grain boundary, forming a lamellar barrier kinetically impeding grain growth to a slow rate. Finally, grains grow by less than 5 nm for higher Pd concentrations where combined solute concentrations exceed 50 at.%. According to our interpretation, the intergranular Pd precipitate barrier may reach a thickness and uniformity here, at which grain growth is largely inhibited. The two characteristic compositions that were characterized for their microstructure in our previous work [25,45] are designated in (f) by a black star ($Pt_{76}Au_{18}Pd_6$) and a black diamond marker ($Pt_{54}Au_{10}Pd_{36}$). The corresponding grain sizes as observed through XRD here and TEM in previous work mutually validate through close agreement. The TEM micrographs and EDX composition maps are shown in Fig. 6. (For interpretation of the references to color in this figure legend, the reader is referred to the web version of this article.)

that both systems have in common under both conditions is the systematic variation of the grain size. As the solute concentration increases, the grain size decreases. This agrees with our expectations for segregation stabilized nanocrystalline systems, in which the preferred grain size is reduced as an increasing amount of solute segregates to the grain boundary. It also conforms to expectations for kinetic pinning of grain boundaries, which should exhibit lower mobility as solute content rises. Such systematic grain size reduction has been widely observed for binary systems, and is now analogously found here for our ternary systems.

As a next step we can compare the grain sizes before and after annealing. In the as-sputtered state, both systems feature a similar grain size distribution across the composition space. After annealing, this distribution remains almost unchanged in Pt−AuAg, whereas in Pt−AuPd the grains have significantly grown. Fig. 5(c and f) present the absolute grain size changes for easy comparison: The grains coarsen negligibly by less than 2 nm in Pt−AuAg, whereas significant coarsening is observed in Pt−AuPd by up to 25 nm.

This pronounced difference in grain coarsening between these two systems is a clear indication of stability differences between them. The Pt−AuAg system displays a high resistance against grain coarsening across all compositions, which indicates excellent thermal stability and confirms our hypothesis developed for this system in the Introduction. The Pt−AuPd system, by contrast, exhibits pronounced coarsening. A closer look at Fig. 5(f) reveals that significant grain growth by about 15−25 nm occurs only on the side of the ternary space, where the Pd concentration is higher than the Au concentration. On the Au-rich side grains typically grow by less than 5 nm. At first glance, this observation is even more surprising considering that according to Table 2 the Pd-rich compositions should have a higher homologous temperature and accordingly feature a higher thermal stability and slower rate of coarsening.

Nonetheless, these observations align with the hypotheses we developed for Pt−AuPd in the Introduction: Au is predicted to be an effective stabilizer, as proven experimentally in previous work [25,58−60] and supported by our findings in Fig. 5c. Accordingly, the Au-rich alloys have a high thermal stability. $Pt_{76}Au_{18}Pd_6$, which in our previous work exhibited a stable grain boundary segregated microstructure [25], appears to fall into this regime (black star marker in Fig. 5f). Pd on the other hand is not an effective stabilizer in its own right. Indeed, Pd can contribute to stabilizing the Pt grain boundary through Au-induced co-segregation and it does so in the Au-rich regime. But being dependent on the presence of Au, Pd fails to do so in the Pd-rich and Au-deficient composition region. Rather, Pd favors phase separation, as demonstrated in our previous work [25] for $Pt_{54}Au_{10}Pd_{36}$, which falls into the region of significant grain growth (black diamond marker in Fig. 5(f)).

For $Pt_{54}Au_{10}Pd_{36}$ we further noted that despite the instability of the nanocrystalline structure, grain growth by only about 20 nm is surprisingly little after 24 h of annealing at 400°C. This we attributed to the formation of Pd precipitate layers, preferentially at the grain boundaries, which kinetically impede grain growth [25]. Based on our data in Fig. 5f, we can extend this interpretation through the following observation: Even on the side of the ternary space that is dominated by Pd solute, grain growth is almost entirely inhibited to less than 5 nm, as the combined solute concentration exceeds 50 at.%. While this seems surprising at first, it may well align with the interpretation of kinetic inhibition of coarsening: With more and more solute available to precipitate, a more uniform and thicker intergranular barrier may be formed, which may thereby become more resistant to migration. Further investigation will be required to elucidate this hypothesis.

Based on the above observations, we draw generalized conclusions for two types of ternary systems displaying distinct stability behavior. This is schematically illustrated in Fig. 6: The first type, a fully stable ternary system, is composed of two stable solvent-solute binaries, with the two solutes not interacting notably, but likely competing for the same grain boundary segregation sites and thus additively contributing to
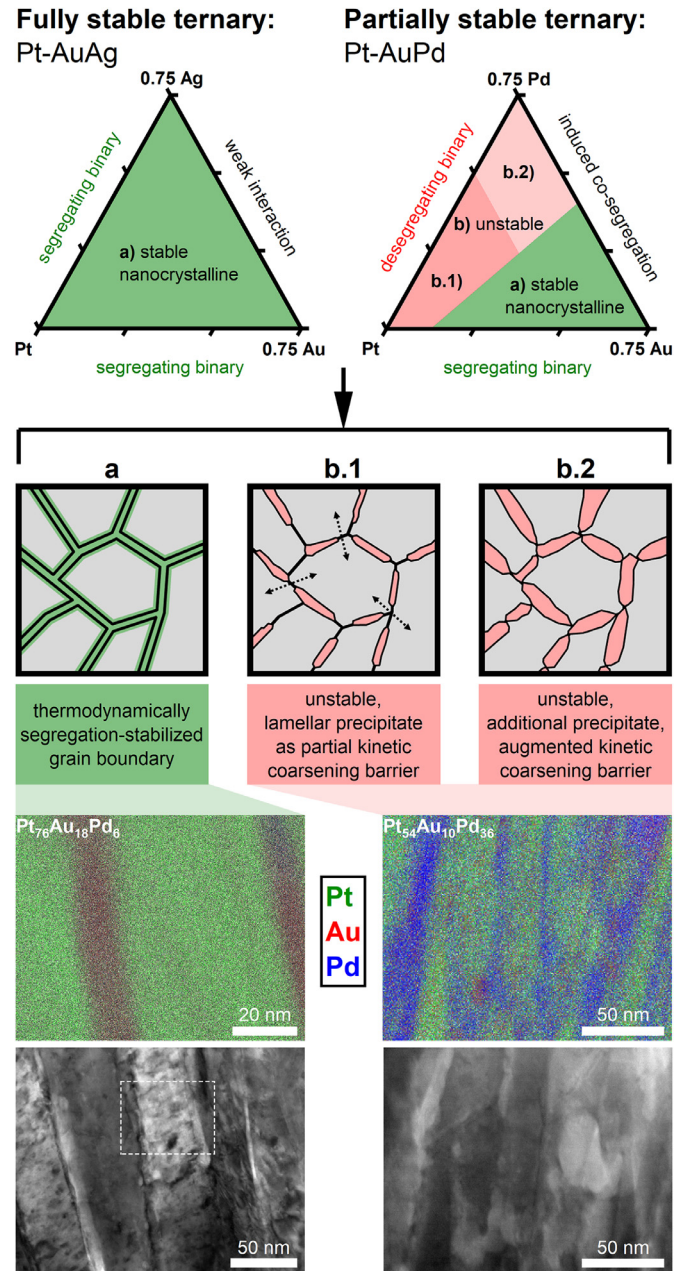

Fig. 6. Schematic summary of the two ternary stability types found in this study. The *fully stable ternary* type exhibits stable solute-segregated nanocrystalline structure across the full composition range, as it is built of two stable underlying solvent-solute binaries. By contrast, the *partially stable ternary* type is built of one stable and one unstable binary. It exhibits stable nanocrystalline structure (region and structure a) only towards the stabilizing solute (here: Au), which segregates to the grain boundary and induces co-segregation of the second solute. The stronger the co-segregation tendency, the more of the second solute can be co-segregated and the wider the stable composition region becomes. Beyond that point (region b), the second solute cannot be retained in the grain boundary and desegregates, forming lamellar precipitates in the intergranular space (structure b.1). These do not stabilize the grain boundary, so the nanocrystalline structure becomes unstable and grains start to grow. The precipitate may, however, act as a kinetic barrier impeding grain growth. For larger amounts of precipitate our data even suggest that the barrier is augmented and more effectively inhibits coarsening (structure b.2). Microstructural characterization via STEM/EDX within the Pt−AuPd system annealed at 400°C was conducted perpendicular to the growth direction on two characteristic compositions in our previous work [25,45]. The micrographs and compositional distribution maps are reprinted here (reprinted with permission) and support our interpretation of the combinatorial data: $Pt_{76}Au_{18}Pd_6$ represents case a), the stable nanocrystalline structure, in which Au segregates to the grain boundary and co-segregates Pd. $Pt_{54}Au_{10}Pd_{36}$ represents case b), the unstable nanocrystalline structure, where in particular Pd forms lamellar precipitates.

nanostructure stability. This type exhibits full stability and minimal grain coarsening across the entire solvent-rich composition space. The second type we find here, a partially stable ternary system, is composed of one stable solvent-solute binary and one unstable binary with a desegregating solute, which can, however, co-segregate as induced by the first solute. This type exhibits two stability regimes. In one, the nanocrystalline structure is stable, since the stabilizing solute segregates and controls the co-segregation of a small quantity of the second solute. In the other, the nanocrystalline structure is not intrinsically stable, because the desegregating solute dominates the overall behavior; it can however form intergranular precipitates that present extreme kinetic barriers for grain growth. Apparently, for larger amounts of lamellar precipitation at grain boundaries, this can even inhibit grain growth altogether.

Clearly, induced co-segregation plays an important role in the partially stable system type: We believe that the magnitude of the tendency to co-segregate determines the extent of the stable nanocrystalline region. With a larger effective enthalpy of co-segregation, more otherwise desegregating solute can be retained in the grain boundary and contribute to stabilizing the nanocrystalline structure. This is an observation uniquely enabled by the efficient experimental approach employed here, and we propose that it would be a desirable next step to explore these modes of stability theoretically across the ternary space.

3.4. Confirmation of grain size variation through SEM

To confirm the trends presented in Fig. 5, SEM micrographs of the film sample surface were recorded and are presented in Fig. 7. These micrographs correspond to samples that were annealed at 400°C with the compositions indicated in Figs. 2 and S1, where a regression was successfully performed. Of course, this SEM analysis cannot provide a complete picture of the sample structure; the appearance of the film sample surface is not necessarily representative of the sample in its entirety, unlike XRD which provides averages from multiple grains at any depth of the film. Nonetheless, the micrographs obtained confirm our previous observations.

Overall, the nano-sized grains observed in the micrographs exhibit sizes closely agreeing with the Scherrer sizes presented in Fig. 5.
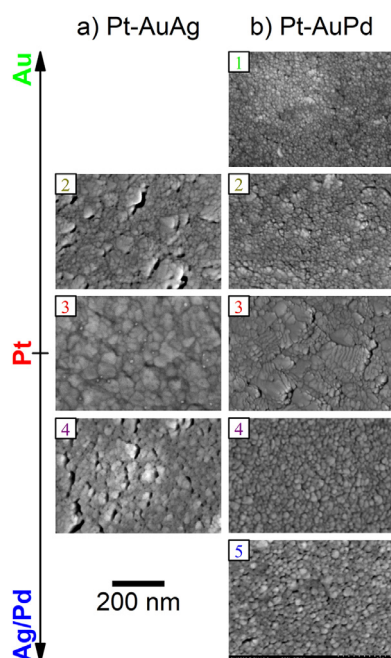

Fig. 7. SEM micrographs of alloys annealed at 400°C with compositions designated in Figs. 2 and S1. The observed grain sizes agree with the Scherrer sizes determined in our XRD analysis (Fig. 5). The grains grow finer with increasing solute concentration. Pd, however, is notably ineffective at producing smaller grains, which agrees with our overall findings. All micrographs were recorded at a magnification of 200k, except for (a.3), which was recorded at 100k and digitally magnified to 200k for direct comparison.

Further, with increasing solute concentration the grain size decreases, as the grains become finer and the surface roughness decreases. Finally, even the three solutes affect the film appearance in different ways, which are in agreement with our above findings. While increasing concentrations of Au and Ag lead to a decrease in grain size, this effect is not as pronounced for Pd, which is manifested particularly when comparing between the coarse grains in micrograph b.5 and the fine grains in micrograph b.1. Overall, we conclude that these SEM observations corroborate the findings from our XRD analysis.

4. Conclusions

A combinatorial co-sputtering technique was used to study the thermal stability of nanocrystalline structure in two ternary alloy systems. These represent two distinct generalized scenarios of nanocrystalline stability in ternary systems. For Pt−AuAg, both solutes independently produce a stable nanocrystalline structure through grain boundary segregation within their respective underlying solvent-solute binary systems. Further, no significant solute-solute interaction exists. Our data reveal that such systems exhibit high nanocrystalline stability across the full ternary composition range. In the second system, Pt−AuPd, only one solute segregates to produce a stable nanocrystalline structure in its binary, while the second solute does not. Further, the stabilizing solute can induce co-segregation of the second solute by increasing its effective segregation enthalpy. Our data reveal that such ternary systems exhibit two stability regimes. Thermodynamically stable nanocrystalline structures are found where the stabilizing solute dominates and retains a smaller amount of the second solute in the grain boundary by inducing its co-segregation. In the other regime, the nanocrystalline structure becomes unstable where the desegregating solute dominates and precipitates, as it cannot be retained in the grain boundary. Induced by the co-segregating solute-solute interaction, however, such precipitates can form as uniform intergranular lamella and act as kinetic barrier against grain growth. In fact, our data suggest that with larger amounts of precipitate this barrier can entirely inhibit grain growth. We argue that the extent of the two stability regimes is determined by the magnitude of the co-segregating interaction, i.e. the region of stable nanocrystalline structure is expected to extend across a wider composition range for systems with a stronger co-segregation tendency between the solutes. The exact position of the boundary line separating the two regimes in the composition space is efficiently revealed using the combinatorial approach chosen here.

Declaration of Competing Interest

The authors declare that they have no known competing financial interests or personal relationships that could have appeared to influence the work reported in this paper.

Supplementary materials

Supplementary material associated with this article can be found in the online version at doi:10.1016/j.actamat.2020.01.059.

References

[1] H. Gleiter, Nanocrystalline Materials, Advanced Structural and Functional Materials, Springer, 1991, pp. 1–37.

[2] A. Inoue, Preparation and novel properties of nanocrystalline and nanoquasicrystalline alloys, Nanostruct. Mater. 6 (1–4) (1995) 53–64.

[3] T. Chookajorn, H.A. Murdoch, C.A. Schuh, Design of stable nanocrystalline alloys, Science 337 (6097) (2012) 951–954.

[4] T. Watanabe, S. Tsurekawa, The control of brittleness and development of desirable mechanical properties in polycrystalline systems by grain boundary engineering, Acta Mater. 47 (15/16) (1999) 4171–4185.

[5] T. Shen, R. Schwarz, S. Feng, J. Swadener, J. Huang, M. Tang, J. Zhang, S. Vogel, Y. Zhao, Effect of solute segregation on the strength of nanocrystalline alloys: inverse Hall−Petch relation, Acta Mater. 55 (15) (2007) 5007–5013.

[6] S. Bechtle, M. Kumar, B.P. Somerday, M.E. Launey, R.O. Ritchie, Grain-boundary engineering markedly reduces susceptibility to intergranular hydrogen embrittlement in metallic materials, Acta Mater. 57 (14) (2009) 4148–4157.

[7] H.-P. Chen, R.K. Kalia, E. Kaxiras, G. Lu, A. Nakano, K.-I. Nomura, A.C.T. van Duin, P. Vashishta, Z. Yuan, Embrittlement of metal by solute segregation-induced amorphization, Phys. Rev. Lett. 104 (15) (2010) 155502.

[8] J. Luo, H. Cheng, K.M. Asl, C.J. Kiely, M.P. Harmer, The role of a bilayer interfacial phase on liquid metal embrittlement, Science 333 (6050) (2011) 1730–1733.

[9] A. Argon, S. Yip, The strongest size, Philos. Mag. Lett. 86 (11) (2006) 713–720.

[10] J.R. Trelewicz, C.A. Schuh, The Hall−Petch breakdown at high strain rates: optimizing nanocrystalline grain size for impact applications, Appl. Phys. Lett. 93 (17) (2008) 171916.

[11] K. Lu, L. Lu, S. Suresh, Strengthening materials by engineering coherent internal boundaries at the nanoscale, Science 324 (5925) (2009) 349–352.

[12] J. Weertman, D. Farkas, K. Hemker, H. Kung, M. Mayo, R. Mitra, H. Van Swygenhoven, Structure and mechanical behavior of bulk nanocrystalline materials, Mrs. Bull. 24 (2) (1999) 44–53.

[13] J. Bauer, M. Seeger, A. Zern, H. Kronmüller, Nanocrystalline FeNdB permanent magnets with enhanced remanence, J Appl Phys 80 (3) (1996) 1667–1673.

[14] T. Schrefl, J. Fidler, H. Kronmüller, Remanence and coercivity in isotropic nanocrystalline permanent magnets, Phys. Rev. B 49 (9) (1994) 6100.

[15] R. Fischer, T. Schrefl, H. Kronmüller, J. Fidler, Grain-size dependence of remanence and coercive field of isotropic nanocrystalline composite permanent magnets, J. Magn. Magn. Mater. 153 (1/2) (1996) 35–49.

[16] G. Herzer, Soft magnetic nanocrystalline materials, Scr. Metal. Mater. 33 (10/11) (1995) 1741–1756.

[17] M.G. Kanatzidis, The Role of Solid-State Chemistry in the Discovery of New Thermoelectric Materials, Semiconductors and Semimetals, Elsevier, Amsterdam, 2001, pp. 51–100.

[18] C. Uher, Skutterudites: Prospective Novel Thermoelectrics, Semiconductors and Semimetals, Elsevier, Amsterdam, 2001, pp. 139–253.

[19] I. Terasaki, Y. Ishii, D. Tanaka, K. Takahata, Y. Iguchi, Thermoelectric properties of NACO$_{2−x}$Cu$_x$O$_4$ improved by the substitution of Cu for Co, Jpn. J. Appl. Phys. 40 (1A) (2001) L65.

[20] J.R. Trelewicz, C.A. Schuh, Grain boundary segregation and thermodynamically stable binary nanocrystalline alloys, Phys. Rev. B 79 (9) (2009) 094112.

[21] J. Weissmüller, Alloy effects in nanostructures, Nanostruct. Mater. 3 (1–6) (1993) 261–272.

[22] J. Weissmüller, Alloy thermodynamics in nanostructures, J. Mater. Res. 9 (1) (1994) 4–7.

[23] T. Chookajorn, C.A. Schuh, Thermodynamics of stable nanocrystalline alloys: a Monte Carlo analysis, Phys. Rev. B 89 (6) (2014) 064102.

[24] A.R. Kalidindi, C.A. Schuh, Stability criteria for nanocrystalline alloys, Acta Mater. 132 (2017) 128–137.

[25] W. Xing, S.A. Kube, A.R. Kalidindi, D. Amram, J. Schroers, C.A. Schuh, Stability of ternary nanocrystalline alloys in the Pt−Pd−Au system, Materialia 8 (2019) 100449.

[26] R. Kirchheim, Grain coarsening inhibited by solute segregation, Acta Mater. 50 (2) (2002) 413–419.

[27] A.J. Detor, C.A. Schuh, Tailoring and patterning the grain size of nanocrystalline alloys, Acta Mater. 55 (1) (2007) 371–379.

[28] K. Darling, M. Tschopp, R. Guduru, W. Yin, Q. Wei, L. Kecskes, Microstructure and mechanical properties of bulk nanostructured Cu−Ta alloys consolidated by equal channel angular extrusion, Acta Mater. 76 (2014) 168–185.

[29] K. Darling, M. Rajagopalan, M. Komarasamy, M. Bhatia, B. Hornbuckle, R. Mishra, K. Solanki, Extreme creep resistance in a microstructurally stable nanocrystalline alloy, Nature 537 (7620) (2016) 378.

[30] A.R. Kalidindi, T. Chookajorn, C.A. Schuh, Nanocrystalline materials at equilibrium: a thermodynamic review, JOM 67 (12) (2015) 2834–2843.

[31] M. Guttmann, Grain boundary segregation, two dimensional compound formation, and precipitation, Metal. Trans. A 8 (1977) 1383–1401.

[32] D. Amram, C.A. Schuh, Interplay between thermodynamic and kinetic stabilization mechanisms in nanocrystalline Fe−Mg alloys, Acta Mater. 144 (2018) 447–458.

[33] M. Park, C.A. Schuh, Accelerated sintering in phase-separating nanostructured alloys, Nat. Commun. 6 (2015) 6858.

[34] M. Seah, Grain boundary segregation and the TT dependence of temper brittleness, Acta Metal. 25 (3) (1977) 345–357.

[35] A. Tabor, J. Thorlin, J. Wallance, In-plain carbon steel fluence of composition on temper brittleness in alloy steels, Trans. ASM 42 (1950) 1033.

[36] M. Baeyertz, W. Craig, J. Sheehan, The effects of molybdenum and commercial ranges of phosphorus upon the toughness of manganese steels containing 0.40 pct carbon, JOM 2 (2) (1950) 389–396.

[37] H. Suto, Y. Yamanouchi, Intergranular fracture and grain boundary segregation in P and Mo bearing 0.6% C steels tempered at low temperature, J. Jpn. Inst. Met. 42 (11) (1978) 1122–1126.

[38] J. Takahashi, J. Haga, K. Kawakami, K. Ushioda, Observation of co-segregation of titanium and boron at the interface between recrystallized and unrecrystallized grains in cold-rolled interstitial-free steel sheets, Ultramicroscopy 159 (2015) 299–307.

[39] W. Xing, A.R. Kalidindi, C.A. Schuh, Preferred nanocrystalline configurations in ternary and multicomponent alloys, Scr. Mater. 127 (2017) 136–140.

[40] P. Lejček, Effect of ternary solute interaction on interfacial segregation and grain boundary embrittlement, J. Mater. Sci. 48 (14) (2013) 4965–4972.

[41] M. Guttmann, P. Dumoulin, M. Wayman, The thermodynamics of interactive co-segregation of phosphorus and alloying elements in iron and temper-brittle steels, Metal. Trans. A 13 (10) (1982) 1693–1711.

[42] P. Lejček, M. Všianská, M. Šob, Recent trends and open questions in grain boundary segregation, J. Mater. Res. 33 (18) (2018) 2647–2660.

[43] P. Lejček, S. Hofmann, Prediction of binary interaction coefficients in grain boundary segregation, Surf. Interf. Anal. 50 (6) (2018) 640–647.

[44] P. Lejček, S. Hofmann, Segregation enthalpies of phosphorus, carbon and silicon at {013} and {012} symmetrical tilt grain boundaries in an Fe-3.5 at.% Si alloy, Acta Metal. Mater. 39 (10) (1991) 2469–2476.

[45] W. Xing, A.R. Kalidindi, D. Amram, C.A. Schuh, Solute interaction effects on grain boundary segregation in ternary alloys, Acta Mater. 161 (2018) 285–294.

[46] J. Cui, Y.S. Chu, O.O. Famodu, Y. Furuya, J. Hattrick-Simpers, R.D. James, A. Ludwig, S. Thienhaus, M. Wuttig, Z. Zhang, Combinatorial search of thermoelastic shape-memory alloys with extremely small hysteresis width, Nat. Mater. 5 (4) (2006) 286.

[47] R. Zarnetta, R. Takahashi, M.L. Young, A. Savan, Y. Furuya, S. Thienhaus, B. Maaß, M. Rahim, J. Frenzel, H. Brunken, Identification of quaternary shape memory alloys with near-zero thermal hysteresis and unprecedented functional stability, Adv. Funct. Mater. 20 (12) (2010) 1917–1923.

[48] S.A. Kube, S. Sohn, D. Uhl, A. Datye, A. Mehta, J. Schroers, Phase selection motifs in high entropy alloys revealed through combinatorial methods: large atomic size difference favors BCC over FCC, Acta Mater. 166 (2019) 677–686.

[49] P. Bordeenithikasem, J. Liu, S.A. Kube, Y. Li, T. Ma, B.E. Scanley, C.C. Broadbridge, J.J. Vlassak, J.P. Singer, J. Schroers, Determination of critical cooling rates in metallic glass forming alloy libraries through laser spike annealing, Sci. Rep. 7 (1) (2017) 7155.

[50] W. Wolf, S.A. Kube, S. Sohn, Y. Xie, J.J. Cha, B.E. Scanley, C.S. Kiminami, C. Bolfarini, W.J. Botta, J. Schroers, Formation and stability of complex metallic phases including quasicrystals explored through combinatorial methods, Sci. Rep. 9 (1) (2019) 7136.

[51] A. Datye, S.A. Kube, D. Verma, J. Schroers, U.D. Schwarz, Accelerated discovery and mechanical property characterization of bioresorbable amorphous alloys in the Mg−Zn−Ca and the Fe−Mg−Zn systems using high-throughput methods, J. Mater. Chem. B 7 (35) (2019) 5392–5400.

[52] S. Ding, Y. Liu, Y. Li, Z. Liu, S. Sohn, F.J. Walker, J. Schroers, Combinatorial development of bulk metallic glasses, Nat. Mater. 13 (5) (2014) 494.

[53] F. Ren, L. Ward, T. Williams, K.J. Laws, C. Wolverton, J. Hattrick-Simpers, A. Mehta, Accelerated discovery of metallic glasses through iteration of machine learning and high-throughput experiments, Sci. Adv. 4 (4) (2018).

[54] J.M. Gregoire, C. Xiang, X. Liu, M. Marcin, J. Jin, Scanning droplet cell for high throughput electrochemical and photoelectrochemical measurements, Rev. Sci. Instrum. 84 (2) (2013) 024102.

[55] J.M. Gregoire, P.J. McCluskey, D. Dale, S. Ding, J. Schroers, J.J. Vlassak, Combining combinatorial nanocalorimetry and X-ray diffraction techniques to study the effects of composition and quench rate on Au−Cu−Si metallic glasses, Scr. Mater. 66 (3) (2012) 178–181.

[56] J.M. Gregoire, D. Dale, A. Kazimirov, F.J. DiSalvo, R.B.v. Dover, High energy X-ray diffraction/X-ray fluorescence spectroscopy for high-throughput analysis of composition spread thin films, Rev. Sci. Instrum. 80 (12) (2009) 123905.

[57] M. Li, J. Gazquez, A. Borisevich, R. Mishra, K.M. Flores, Evaluation of microstructure and mechanical property variations in Al$_x$CoCrFeNi high entropy alloys produced by a high-throughput laser deposition method, Intermetallics 95 (2018) 110–118.

[58] H.A. Murdoch, C.A. Schuh, Estimation of grain boundary segregation enthalpy and its role in stable nanocrystalline alloy design, J. Mater. Res. 28 (16) (2013) 2154–2163.

[59] J.F. Curry, T.F. Babuska, T.A. Furnish, P. Lu, D.P. Adams, A.B. Kustas, B.L. Nation, M.T. Dugger, M. Chandross, B.G. Clark, Achieving ultralow wear with stable nanocrystalline metals, Adv. Mater. 30 (32) (2018) 1802026.

[60] F. Abdeljawad, P. Lu, N. Argibay, B.G. Clark, B.L. Boyce, S.M. Foiles, Grain boundary segregation in immiscible nanocrystalline alloys, Acta Mater. 126 (2017) 528–539.

[61] Vol. F.d. Boer, R. Boom, W. Mattens, A. Miedema, A. Niessen, in: F.R. de Boer, D.G. Pettifor (Eds.), Cohesion in metals: transition metal alloys, 1, North Holland, Amsterdam, Netherlands, 1988. Vol. (series eds.).

[62] A. Miedema, Surface segregation in alloys of transition-metals, Zeitschrift Fur Metallkunde 69 (7) (1978) 455–461.

[63] J. Darby Jr, The relative heats of formation of solid gold-palladium alloys, Acta Metal. 14 (3) (1966) 265–270.

[64] W. Yim, R. Paff, Thermal expansion of AlN, sapphire, and silicon, J. Appl. Phys. 45 (3) (1974) 1456–1457.

[65] D.R. Lide, CRC Handbook of Chemistry and Physics, CRC Press, Boca Raton, FL, 2005 Internet Version 2005.

[66] A. Takeuchi, A. Inoue, Classification of bulk metallic glasses by atomic size difference, heat of mixing and period of constituent elements and its application to characterization of the main alloying element, Mater. Trans. 46 (12) (2005) 2817–2829.

[67] W.D. Callister, D.G. Rethwisch, Materials Science and Engineering, Wiley, Hoboken, NJ, 2015.

[68] P. Scherrer, Nachr GES wiss goettingen, Math. Phys. 2 (1918) 98–100.

[69] J.I. Langford, A. Wilson, Scherrer after sixty years: a survey and some new results in the determination of crystallite size, J. Appl. Crystallogr. 11 (2) (1978) 102–113.

[70] U. Holzwarth, N. Gibson, The Scherrer equation versus the 'Debye-Scherrer equation', Nat. Nanotechnol. 6 (9) (2011) 534.